SAND2018-9986J

CO_2 charged brines changed rock strength and stiffness at Crystal Geyser, Utah: Implications for leaking subsurface CO_2 storage reservoirs

Espinoza, D. Nicolas[1*]; Jung, Hojung[1]; Major, Jonathan R.[2]; Sun, Zhuang[1]; Ramos, Matthew J.[2]; Eichhubl, Peter[2]; Balhoff, Matthew T.[1]; Choens, R. Charles[3]; Dewers, Thomas A.[3]

*corresponding author: espinoza@austin.utexas.edu, 200 E. Dean Keeton, Austin 78712, USA

(1) Department of Petroleum and Geosystems Engineering, The University of Texas at Austin

(2) Bureau of Economic Geology, Jackson School of Geosciences, The University of Texas at Austin

(3) Geomechanics Department, Sandia National Laboratories

KEY POINTS

- Changes in rock strength and deformational behavior imparted by mineral dissolution and precipitation can impact trapping of buoyant fluids
- Experimental evidence shows that seepage of CO_2-charged brine causes reduction of shear strength and strain-softening of Entrada sandstone and Summerville siltstone samples, and stiffening of Mancos shale
- Numerical simulations confirm the role of cement size alteration as one of the main controls for sandstone chemo-mechanical alteration and predict vertical compaction and lateral stress relaxation in the event of cement dissolution under in-situ subsurface conditions

Abstract

CO_2 geological storage in saline aquifers results in acidification of resident brine. Chemical reactions between acidified brine and rock minerals lead to dissolution and precipitation of minerals at various time scales. Mineral dissolution and precipitation are often neglected in assessing the mechanical integrity of target storage formations, yet, changes in rock strength and deformational behavior can impact trapping mechanisms. This study shows the impact of exposure to CO_2-charged brine on shear strength and stiffness of various outcrop rocks evaluated through triaxial testing. The tested rocks were exposed to CO_2-charged brine over geological time at a naturally occurring near-surface seepage along the Little Grand Wash Fault and Salt Wash Grabens, which include the Crystal Geyser site near the town of Green River, Utah. Prior work suggests that this site provides a near-surface structural analog for possible fault-controlled CO2 leakage over time scales that exceed expected injection time scales (10-100 years). Results show mechanical alteration in various aspects: (1) CO_2-charged brine alteration at near-surface conditions results in mineral dissolution/precipitation and reduction of shear strength and brittleness of Entrada sandstone and Summerville siltstone samples, and (2) carbonate precipitation in fractured Mancos shale leads to matrix stiffening and fracture mineralization resulting in overall stiffer and likely tighter shale. Additional discrete element simulations coupled with a bonded-particle-model confirm the role of cement bond size alteration as one of the main controls for rock chemo-mechanical alteration in sandstones. The chemo-mechanical alteration path that mimics cement dissolution (under stressed subsurface conditions) results in vertical compaction and lateral stress relaxation. Overall, results show that rock exposure to CO_2-charged brine can impart distinct petrophysical and geomechanical changes according to rock lithology and location with respect to major CO_2 conduits. While mineral dissolution in the storage rock may result in undesired reservoir strains and changes of stresses, mineral precipitation downstream from a leakage path can help seal potentially induced fractures.

1. Introduction

Large-scale injection of carbon dioxide (CO_2) in deep subsurface formations is an alternative for disposing anthropogenic CO_2 instead of venting to the atmosphere [Pacala and Socolow, 2004]. Natural CO_2 accumulations (stable and seeping) exist in various sedimentary basins, where pore pressure has been documented to vary from below hydrostatic pressure to almost lithostatic stress [Chiodini et al., 1995; Pearce et al., 1996; Heath et al., 2009; Sathaye et al., 2014; Hangx et al., 2015]. Although the oil and gas industry has developed mature technologies for CO_2 injection and enhanced oil recovery, storing large volumes of CO_2 requires careful analyses of all possible implications that may affect effective and long-term CO_2 sequestration [Sharp, 1975; Lake, 1996; Rutqvist et al., 2016].

Carbonic acid is the most common chemical weathering agent on the Earth's crust, resulting from the reaction between atmospheric CO_2 and rainwater [Stumm and Morgan, 2012]. Likewise, the injection of CO_2 in deep geological formations induces geochemical disequilibrium from mixing of CO_2 and resident brine, leading to reactions with minerals in the host rock including potential mineral dissolution/precipitation and clay fabric alteration [Gunter et al., 2000; Kaszuba et al., 2005; McGrail et al. 2009; Espinoza and Santamarina, 2012; Yoksoulian et al., 2013]. The extent of acidification increases with CO_2 pressure and CO_2 solubility in brine, and reaches a plateau around the CO_2 critical pressure [Duan and Sun, 2003; Spycher et al., 2003]. Chemical reactions may occur in the reservoir/storage rock, the caprock, well-cement interfaces, and in fault gouge material, if contacted by CO_2. Advective processes control reactions in the reservoir rock (including density-driven convection caused by CO_2 dissolution into brine), while diffusion mechanisms control reactions in the caprock (in the absence of connected fractures) [Gaus et al., 2005; Xu et al., 2005; Kneafsey and Pruess, 2010; Hangx et al., 2010; Rutqvist et al., 2016].

Dissolution and precipitation of minerals due to CO_2 injection can alter rock petrophysical and geomechanical properties [Vanorio et al., 2011; Major et al., 2014; Rohmer et al., 2016]. Such alterations depend on the amount of reacted minerals and where dissolution and precipitation take place in the pore structure. For example, precipitation of small mineral amounts in pore throats instead of pore bodies can have a significant effect on permeability and capillary pressure [Ross et al., 1982; Chiodini et al., 1995; Benavente et al., 2004]. Predominantly quartzitic sandstones and unconsolidated sands are expected to have minor chemo-mechanical alteration when exposed to CO_2 due to a lack of reactive minerals. Sandstones with "CO_2-weak" intergranular cements appear to be the most easily alterable type of rock with respect to geomechanical properties, as even minor alterations can have a large impact on

77 geomechanical properties dependent on cementation. Dissolution and degradation of load-bearing
78 cements can lead to (1) decreases of cohesive strength, fracture toughness, and yield stress locus size, (2)
79 increases of compliance and creep, (3) changes in post-peak behavior, and (4) changes in frictional
80 behavior [Fernandez and Santamarina, 2001; Bemer and Lombard, 2010; Xie et al., 2011; Zinsmeister et
81 al., 2013; Major et al., 2014; Bakker et al., 2016; Rinehart et al., 2016; Sun et al., 2016a]. Examples of these
82 types of rock include carbonate-cemented sandstones (e.g., Entrada sandstone, Castlegate sandstone),
83 and clay-cemented sandstones (Chlorite-cemented Tuscaloosa sandstone and Mt. Simon sandstone)
84 [Yoksoulian et al., 2013; Rinehart et al., 2016; Major et al., in review]. Grain-supported carbonate rocks
85 such as chalks can suffer significant strains when exposed to CO_2-acidified brine [Liteanu et al., 2013],
86 while matrix-supported carbonate rocks can undergo significant pore enlargement with modest effects
87 on rock mechanical properties until large amounts of rock are dissolved [Fredd and Fogler, 1998; Carroll
88 et al., 2013]. Rocks with patchy or laminated distribution of dissolvable minerals, such as carbonate-rich
89 shales, stand in between dissolvable-matrix rocks and dissolvable-cement sandstones [Shovkun and
90 Espinoza, 2017]. Core-scale experimental results investigating CO_2 reactions in shale caprocks are limited
91 due to the inherent difficulties in machining and flowing fluids through such tight and fragile lithologies
92 [Ilgen et al., in review]. Design of CO_2 injection projects often neglects chemically-induced strains and
93 stresses, however, coupled chemo-mechanical processes can affect short-term injection response and
94 long-term trapping mechanisms in CO_2 geological storage. Examples of coupled processes induced by
95 mineral dissolution include changes in wellbore injectivity, reservoir compaction, and lateral stress
96 relaxation [Ross et al. 1982; Oudinot et al., 2011; Shin et al., 2008; Stefanou and Sulem, 2014; Shovkun
97 and Espinoza, 2017].

98 In this study, we investigate the changes in geomechanical properties caused by CO_2-charged brine over
99 geologic time from rocks in a sedimentary system accessible in outcrops at the Crystal Geyser field site.
100 First, we present an overview of the Crystal Geyser site, rock diagenetic history, and diagenesis triggered
101 by seepage of CO_2-rich brine from a natural CO_2 source along faults. Second, we show and discuss
102 experimental results from triaxial testing of rock specimens unaltered and altered by CO_2-charged brine,
103 i.e., rock stress-strain behavior and shear strength. A systematic investigation of mode-1 fracture
104 propagation in the same rock samples is outside the scope of this study and will be reported in a separate
105 paper. The triaxial testing results are complemented by microphotographs, SEM-EDS, and X-ray
106 microtomographic observations to understand how alteration and heterogeneities affect strain
107 localization and micromechanical failure processes. Third, we introduce the application of discrete
108 element modeling to understand particle-level mechanisms responsible for the mechanical alteration of

the tested sandstone samples. The article finishes with a comparison of alteration paths expected on surface outcrops and under subsurface in-situ conditions.

2. Crystal Geyser: Geological setting, rock diagenetic history, and sampling

The Crystal Geyser field site near the town of Green River in eastern Utah has been widely utilized as a CO_2 sequestration analog [e.g. Heath et al., 2009; Wilkinson et al., 2009; Burnside et al., 2013]. Here, CO_2-charged brine sourced from rocks in the deep subsurface Paradox Basin migrates up along normal faults, including the Little Grand Wash Fault, and mixes with meteoric water from the shallower Navajo aquifer before reaching the surface in a series of fault-related seeps or through a small number of abandoned wells [Wilkinson et al., 2009]. The roughly E-W striking normal faults dominantly dip southward and cut a series of Mesozoic siliciclastic rocks within the broad, gently northward plunging Green River Anticline [Dockrill and Shipton, 2010]. A series of actively precipitating and fossil travertine mounds paralleling the normal faults are products of the CO_2 seeps active for at least 400 ka [Burnside et al., 2013].

The Little Grand Wash Fault near Crystal Geyser exposes primarily the Jurassic Summerville Formation, a marginal marine siltstone with carbonate and mudstone beds, and the Morrison Formation, including the Brushy Basin (dominantly mudstone) and Salt Wash (dominantly coarse-grained sandstone interbedded with mudstone) members. The Cretaceous Mancos shale is exposed in the hanging wall. The Salt Wash Graben located 10 km to the south of Little Grand Wash exposes units slightly lower in the stratigraphic section including the Jurassic Entrada Sandstone. All these units have been altered in the vicinity of the fault, resulting mostly in hematite dissolution and calcite precipitation that has been attributed to CO_2-brine-rock interactions [Urquhart, 2011; Wigley et al., 2012; Major et al., 2014, in review]. Localized calcite precipitation in the vicinity to faults has been attributed to CO_2 degassing of ascending CO_2-charged brine [Urquhart, 2011].

Rock samples selected for this study include both CO_2-altered (bleached) and unaltered (red) Entrada sandstone, CO_2-altered and unaltered Summerville Formation siltstones, and CO_2-altered and relatively unaltered Mancos shale. Altered/unaltered sample pairs were taken from outcrops (either adjacent to each other or from similar stratigraphic levels) in near and far proximity to the fault and travertine mounds (See details in Table 1 and locations in triangles in Figure 1). The field sampling strategy was based on recognition of bleaching and/or proximity to conduits (i.e. travertine mounds), then confirmed analytically by XRD and petrologic analyses. All samples were retrieved from blocks excavated in the sampling points

about 10 cm away from the surface to minimize alterations from surface weathering. The following petrographic description corresponds to rocks sampled at the locations shown in Figure 1.

Entrada sandstone: Unaltered entrada sandstone at Crystal Geyser consists of eolian dune deposits of well-sorted fine-to-medium grained reddish sandstone (~55 wt% Quartz, 24 wt% clays, 14 wt% carbonates, 7 wt% K-feldspar, plus trace minerals). Burial and diagenesis resulted in sub-angular to rounded grains with development of hematite, goethite, and illite-smectite grain coatings. Primary carbonates take about 5.5%wt of mineral composition in the form of sparry calcite. Flow of CO_2-charged brine resulted in bleaching of red Entrada Sandstone causing hematite dissolution (with ensuing trace metal mobilization), dissolution of preexisting carbonate and silicate minerals and formation of secondary clays and carbonates [Wigley et al., 2012].

Summerville Siltstone: Unaltered Summerville siltstone is a reddish siltstone with minor shale and limestone beds. The siltstone matrix is composed by very fine-grained quartz grains in a matrix formed principally by sparry calcite, illite-smectite, and feldspar; natural heterogeneity results in variations of carbonate content from 23 wt% to 43 wt% [Aman et al., 2017; Major et al., 2014]. Samples of altered Summerville siltstone collected in the proximity of faults and below travertine mounds exhibit similar amounts of carbonate content but cementation is in the form of fine-grained micritic calcite and clays. Altered Summerville samples also have a distinct color with respect to unaltered Summerville as a result of bleaching and changes in mineralogy. In addition, some altered samples exhibit mineralized veins (example in Figure 5).

Mancos Shale: Mancos Shale is a regionally extensive gray marine shale, with a few silty layers exposed near the field site. Samples of Mancos Shale collected far from CO_2 springs exhibit a matrix dominated by fine quartz (64 wt%), feldspar and clay minerals (illite, illite/smectite, chlorite/smectite, and kaolinite). Retrieved unaltered Mancos samples exhibited open fractures likely resulting from a combination of surface exhumation and sample preparation (Figure 7). In contrast, Mancos Shale samples retrieved in proximity to faults exhibit large amounts of matrix calcite (~50 wt%) with decreased amount of clay minerals. At larger scales, altered Mancos shale shows straight mm-thick mineralized veins separated by ~0.5 m. Despite the presence of these discontinuities, the retrieved altered Mancos samples did not show any open fractures observable with the X-ray microtomograph.

3. Triaxial testing

3.1. Rock samples

Table 2 summarizes details from all samples tested and experiments conducted. All samples are cylindrical and have a nominal diameter of 25 mm. Entrada and Summerville samples were prepared to have a length to diameter ratio between 2:1 and 2.5:1 consistent with material testing standards (ASTM D7012). Mancos shale samples were limited in quantity and size; the tallest unaltered Mancos shale available for testing is 34.8 mm. Short samples are significantly affected by shear friction at loading caps, while long samples may present buckling instabilities under axial compression.

3.2. Triaxial frame and deviatoric loading procedure

We conducted tests in an ultra-stiff (10^7 N/mm) triaxial frame manufactured by TerraTek and equipped with local strain transducers (set of cantilever arms) to measure bulk axial and radial strains. Servo-hydraulic systems control confining stress σ_3 and deviatoric stress σ_1-σ_3. We conducted two types of tests: standard constant axial strain rate tests at a constant confining stress, and multistage experiments with axial loading at multiple confining stresses utilizing the same sample. Table 2 specifies the type of test run on each sample. Standard tests pursued clear evidence of post-peak behavior. The multistage test consists of stages of deviatoric loading, each one to the onset of sample dilation (based on volumetric strain measurements) before unloading and reloading at a higher confining stress [Alsalman et al., 2015, Ramos et al., 2017]. Multistage triaxial tests are useful to define the failure envelope with a limited number of samples. Short unloading paths served to measure elastic rock rebound and characteristic elastic coefficients. All samples were air-dry, hence, pore pressure is negligible and all reported stresses are Terzaghi effective stresses. Deviatoric loading proceeded at an axial strain rate of $4 \cdot 10^{-6}$ s^{-1} in all tests. We chose effective confining stresses equal to 0.69 MPa (100 psi), 6.9 MPa (1,000 psi), and 20.7 MPa (3,000 psi) for our triaxial tests based on typical values to study friction-strengthening behavior of geomaterials and potential brittle to ductile transition in sandstones and shales. A confining stress of 6.9 MPa is more or less equivalent to a horizontal effective stress developed at about 1.6 km of depth in an on-shore sedimentary basin with hydrostatic pore pressure and no tectonic strains.

Data reduction utilizes a linear Coulomb criterion to characterize shear strength, such that,

$$\sigma_1(\text{peak}) = UCS + q \cdot \sigma_3 \quad (1)$$

where *UCS* is the unconfined compressive strength, q is a friction parameter, and φ is the friction angle, such that $q = (1+\sin\varphi)/(1-\sin\varphi)$. The *UCS* [MPa] quantifies the level of cementation strength in the sample and φ [-] quantifies the increase in rock shear strength due to effective mean compressive stresses [Jaeger et al., 2009]. We calculate Young's modulus E and Poisson's ratio ν assuming material isotropy:

$$E = \frac{\Delta\sigma_1}{\Delta\varepsilon_1}\bigg|_{\sigma_3} \quad (2)$$

$$\nu = -\frac{\Delta\varepsilon_3}{\Delta\varepsilon_1}\bigg|_{\sigma_3} \quad (3)$$

where ε_1 and ε_3 are the strains along the maximum and least principal directions. The Young's modulus E [GPa] quantifies the stiffness of the rock and is proportional to degree of cementation and grain contact overlap; while ν quantifies strains (and stresses if confined) perpendicular to the applied stress [Gueguen and Palciauskas, 1994]. The reported loading elastic coefficients correspond to tangent measurements before departure from linearity and unloading coefficients correspond to the average of at least two unloading cycles.

3.3. Results

3.3.1. Entrada sandstone

The strain-stress results for standard tests in Entrada sandstone samples at various effective confining stress σ_3 are available in Figure 2a. We discarded two tests in altered Entrada sandstone that showed unexpectedly low peak stress values (σ_1-σ_3 = 21.35 MPa at σ_3 = 6.9 MPa and σ_1-σ_3 = 49.56 MPa at σ_3 = 20.7 MPa) likely due to a failed confinement or a pre-existing weakness induced or not detected before triaxial testing. Unaltered samples appear stronger on average than CO_2-altered bleached samples, although natural heterogeneity contributes to scatter in the data. The tests run at σ_3 = 0.69 MPa show well defined peak stresses followed by rapid strain softening in both unaltered and altered samples. Post-peak behavior of unaltered samples conducted at higher confining stress show rapid strain softening as well. The weakest bleached samples show gradual strain softening after peak stress. Figure 2b shows an average unconfined compression strength reduction (*UCS* – Eq. 1) of about 14% in altered samples in comparison with unaltered samples. The difference in the friction parameter q is about 10%. The experimental data of Entrada Sandstone show dilation (0.8% to 0.4% from onset of dilatancy to peak stress decreasing with confining stress). Dilation is associated with grain rotation and fracture opening rather than grain crushing. Altered Entrada sandstone dilates less than unaltered entrada Sandstone, which

suggests weakening and increased porosity in altered Entrada Sandstone with respect to unaltered Entrada.

Similar to strength trends, a number of CO_2-altered Entrada sandstone samples are softer (lower Young's modulus) than unaltered Entrada (See Figure 2c and Table 2). The loading and unloading Young's moduli of altered rocks are similar but typically lower than the moduli of unaltered rocks (Figure 2c).

Figure 3 shows X-ray micro-tomographic images of samples EU7 and EA6 after testing to peak stress at σ_3 = 20.7 MPa. Strain localization concentrates in two planes at characteristic angles corresponding to shear failure. Careful inspection shows that fractures originating from edges of the sample do not perfectly align but seem to coalesce upon a slight change of direction (top third in EU7 and lower fourth in EA6). Samples tested at lower confining stress exhibit similar patterns with clear shear fractures oriented at about the same angle: 72.4 ± 2.9° in unaltered Entrada samples and 72.2 ± 3.7° in altered Entrada samples (considers individual fractures, not average after coalescence). Sample heterogeneity mostly comprised of weak lamination does not seem to affect strain localization and damage evolution. High magnification tomographic slices show higher porosity and less cementation in altered samples than in unaltered samples.

3.3.2. Summerville siltstone

Figure 4a shows the strain-stress results from testing Summerville siltstone samples with standard tests at σ_3 = 0.69 MPa (100 psi), and multistage tests at σ_3 = 0.69 MPa (100 psi), 6.9 MPa (1,000 psi), and 20.7 MPa (3,000 psi). Results clearly show a weaker altered Summerville siltstone samples than unaltered samples. Both rock strength and stiffness undergo 7 to 10 fold decrease with rock alteration (See Table 2). Standard tests at σ_3 = 0.69 MPa show clear differences in strength, stiffness, and post-peak behavior between unaltered and altered samples (Figure 4a-c). Multistage testing at various confining stresses confirm marked reduction of rock strength and yield stresses in altered samples. Cohesive strength reduces about 8 fold, yet samples possess similar internal friction angles (Figure 4b).

X-ray micro-tomographic images of Summerville siltstone samples help explain failure patterns (examples SU2 and SA2 in Figure 5). The unaltered sample SU2 shows various planes of failure combining apparent splitting and inclined shear fractures. The presence of multiple fractures likely correspond to small brittle events (rapid drop of deviatoric stress) observed in strain-stress response of unaltered Summerville samples at σ_3 = 0.69 MPa. The altered samples show marked heterogeneities comprised by distinct layers and partially mineralized fractures, some of them which likely associate with proximity to the fault gouge

(Table 1 and Figure 1). These heterogeneities contributed the branching and turning of fractures during failure. Despite an apparent "ductile" stress-strain signature up to $\varepsilon_1 \sim 0.03$, altered Summerville Siltstone samples showed a significant number of fractures, typical of brittle failure. X-ray tomographic inspection of unaltered siltstone samples after multistage testing at various confining stresses do not show observable fractures and discontinuities. This observation suggests that multistage testing did not take unaltered Summerville samples to stresses close to ultimate strength.

3.3.3. Mancos shale

Stress-strain results of Mancos shale samples at confining stress σ_3 = 0.69 MPa (100 psi) show that shale samples exposed to CO_2-charged brine in the vicinity if the fault are stiffer than the unaltered Mancos samples more distal from the fault (Figure 6 and Table 2). The altered samples also exhibit smaller difference of unloading versus loading Young's modulus than altered samples. We limited testing to a predetermined stress for short samples (MU2, MU3, MA2). Indeed, the observed peak stresses for MU1 and MA1 are not suitable for rock strength comparison because the unaltered sample MU1 is too short to yield a reliable value of shear strength. MU2 was also stopped early because of unexpected early dilation. A thorough strength measurement was unattainable due to limitations in successful coring of large samples because of pre-existing open fractures, mostly in the unaltered Mancos shale blocks. Non-optimal sample size also influences the accuracy of measured elastic properties.

Figure 7 shows X-ray micro-tomographic slices of Mancos shale samples before and after failure. Unaltered shale samples have numerous open pre-existing fractures along the bedding plane. Deviatoric loading in MU1 promoted growth of shear fractures that interacted with pre-existing weakness planes. The altered Mancos shale samples do not exhibit open fractures observable with micro-tomography. Altered shale samples have rare, closed sub-mm carbonate-filled veins, and gypsum filled fractures, the latter related to weathering and observed at the outcrop. These observations support higher stiffness observed in CO_2-altered Mancos shale than in unaltered Mancos shale with open fractures. Some open microfractures beyond the resolution of the microtomography may also exist, as evidenced from the stiffening strain-stress response of MA1 (Figure 6). Linkages between open and mineralized fractures are explored in Section 5.

4. Discrete element modeling of cemented sandstone

4.1. Grain-cemented rock model

We apply the discrete element model to mimic the behavior of Entrada Sandstone. This is a reasonable model for grain-cemented sandstones with rounded grains (Figure 3 and Supporting Information 1). The discrete element model (DEM) has been widely used to model the mechanical behavior of geomaterials since the pioneering work of Cundall and Strack [1979]. The bonded-particle model (BPM) approximates grain-cemented rock with spherical particles connected by bonds [Potyondy and Cundall, 2004]. In this study we couple BPM with the discrete element code LIGGGHTS [Kloss et al., 2012]. We present an overview of the numerical model here. The reader can find more details elsewhere [Obermayr et al. 2011, 2013; Sun et al., 2016b].

We idealize the interaction between two cemented particles *i* and *j*, through a spring-damper system where the stiffness, damping and friction coefficient are the parameters of the spring, dashpot and slip mechanism (Figure 8a). The particle force and cement force act in parallel between particles and are decomposed into normal and tangential directions. Bond breakage occurs when either normal or tangential stress exceeds the corresponding bond strength. We utilize a global parameter λ to relate bond size to the radii of particles [Obermayr et al., 2013]. For two arbitrarily connected particles *i* and *j* with radii R_i and R_j, the bond radius $R_{b,ij}$ is

$$R_{b,ij} = \lambda \frac{R_i + R_j}{2} \tag{4}$$

Therefore, λ is a dimensionless parameter that quantifies the amount of cementation and varies from 0 (no cementation) to 1 (full cementation). Realistic bond sizes require $\lambda < 1$.

The model utilizes a randomly generated cylindrical particle pack with particle radii from 25 to 50 µm (uniform size distribution). In our idealization, we disregard the effects of patchy cement distribution and pore-filling dissolvable minerals. The height and diameter of the particle pack are 2.54 mm and 1.27 mm (20 times smaller than actual sample). The sample contains 7,928 particles and 23,178 bonds. Boundary conditions apply a constant radial confining stress and constant axial loading displacement rate. There is no pore pressure in DEM simulations. Table 3 shows the parameters used in the model (result of calibration with Entrada sandstone tests at σ_3 = 0.69 MPa), where E_c [Pa] and E_b [Pa] are the elastic moduli of particle-particle contacts and bonds, k_T [N/m] and k_N [N/m] are the tangential and normal stiffness, μ [-

] is the friction coefficient, σ_c [Pa] and τ_c [Pa] are the bond normal and tangential strength (per unit of normal area). We validated the calibrated parameters with "blind" simulations for σ_3 = 6.9 MPa and 20.7 MPa (Supporting Information 2). Calibration shows that cement dissolution is the variable that matches best indentation, scratch, and triaxial experimental results (opposed to cement strength variation and cement elastic modulus variation - details are available elsewhere: Sun et al. [2016b, 2017; in review]). We do not discard the possible contribution of other factors in changing the geomechanical properties of altered Entrada Sandstone, such as reduction in bond shear strength and pore-filling mineral dissolution – explored in other studies by Shin et al., 2008 and Sun et al. [in review].

4.2. Effects of cement bond size in mechanical response of Entrada Sandstone

Previous studies indicate that weakening of Entrada sandstone after long-term contact with CO_2-acidified brine is likely due to the dissolution of contact cements [Wigley et al., 2012; Major et al., 2014]. In this section, we investigate the impact of bond size on the stress-strain response of digital Entrada Sandstone models subjected to deviatoric loading.

A change of parameter λ from 0.8 to 0.2 mimics the effects of cement size reduction (Figure 8b). Digital rock samples exhibit reduction of shear strength and increased ductility as the bond size decreases. The simulation results mirror experimental observations and indicate that CO_2-related alteration in Entrada sandstone not only can degrade bulk mechanical properties but also lead to a brittle to ductile transition. Other DEM-BPM results show that dissolution of pore filling dissolvable minerals and reduction of bond shear strength can also result in decreased bulk shear strength and increased porosity [Sun et al., in review]. Section 5.3 explores large-scale implications of cement size reduction and its impact on geomechanical integrity of target CO_2 storage formations.

5. Discussion

5.1. Origin of rock mechanical alteration and comparison with previous studies

Entrada sandstone. Previous work suggests dissolution of grain-coating hematite cement as the main factor for bleaching and weakening of Entrada sandstone [Major et al., 2014]. Calcite dissolution and re-precipitation may also affect geomechanical properties. Unaltered and bleached Entrada Sandstone show velocity-strengthening slip behavior, unless significant carbonate precipitation occurs [Bakker et al., 2016]. Both hematite and calcite dissolution are compatible with geochemical reactions in acidic environments [Eichhubl et al., 2004]. Laboratory experiments show that CO_2-charged brine interaction

with unaltered Entrada sandstone can result in localized carbonate dissolution and increases of porosity [Aman et al., 2017]. As expected, there was no sign of pre-existing damage in Entrada samples (observed in X-ray microCT images) induced by the fault shear zone process (samples ~100 m away from fault). Our measurements indicate average porosity increases from 8.3±0.3% to 11.3±0.3% with alteration in Entrada sandstone. Triaxial test results presented here show weakening up to 14% of the unaltered rock stiffness and strength and agree with measurements based on indentation, scratching and double torsion techniques (Supplementary Information 3). A few samples of altered Entrada sandstone are as strong as (or stronger than) unaltered Entrada in triaxial tests (Figure 2). Such variation may be explained by the natural heterogeneity of the sandstone formation but also by variations in calcite dissolution and precipitation (such as in some portions close to the fault [Bakker et al., 2016]). Our results document a small decrease in the internal friction coefficient as well.

Summerville siltstone. Hematite dissolution, calcite dissolution and precipitation as micritic cement, and increased amount of clay cements contribute to the weakening of Summerville siltstone. A significant increase of average porosity (Table 2) from 4.8±1.6% to 10.2±0.4% characterizes altered from unaltered samples. Laboratory studies show localized carbonate dissolution by CO_2-charged brine with ensuing increased porosity in unaltered Summerville Siltstone [Aman et al., 2017]. In addition to changes in the rock matrix, X-ray tomographic images show the presence of mineralized natural fractures in altered Summerville that likely affected rock strength at the core scale (Figure 5). Pre-existing mineralized fractures usually constitute planes of weakness in rocks, because of lower shear and tensile bonding strength than the rock matrix [Gale et al. 2007, Lee et al., 2015]. Pre-existing mineralized fractures may be the result of damage near the fault gouge and such alterations may also contribute to overall weakening of the retrieved altered Summerville samples (~2 m away from fault). The decreases of strength and stiffness up to 87% measured in triaxial tests are consistent with weakening measured through indentation and double torsion testing (Supplementary Information 3). Uncertainties in the determination of peak stress of unaltered Summerville siltstone in multistage testing do not permit unequivocally concluding about alterations of the internal friction angle (samples run only until onset of dilation). Yet, there appears to be little change of the internal friction angle if one disregards the data points at 20.7 MPa (Figure 4). A drop of ~38% in fracture toughness between unaltered and altered Summerville siltstone was observed in double torsion mode-1 fracture mechanics tests by Major et al. [2014].

Mancos Shale. The unaltered Mancos shale samples are softer than the altered samples. One cause contributing to softening is the presence of pre-existing open fractures in unaltered shale as shown in X-ray tomography slices (Figure 7). The increase of stiffness up to +434% of altered Mancos with respected to unaltered –yet fractured– Mancos may be also aided by changes in the shale matrix. XRD analysis indicates calcite content increases by up to 50 wt% in altered samples in comparison to unaltered samples, the latter with much lower calcite amounts and higher clay content. The increased calcite content (Table 1) coincides with higher measured values of fracture toughness [Major et al., 2014].

5.2. Challenges of comparing mechanical properties of CO_2 naturally altered and unaltered rock outcrop samples

Our experimental results show evidence of differences in geomechanical properties between comparable rock lithofacies that have been exposed and unexposed to CO_2-charged brine. There is clear evidence of induced diagenesis by CO_2-charged brine on Crystal Geyser lithofacies [Wigley et al. 2012, Burnside et al. 2013]. Some factors that could add uncertainty to the direct influence of CO_2-induced diagenesis in our comparison include the natural spatial variability of sedimentary rocks in vertical and horizontal direction, the presence of events that may postdate CO_2 alteration, the proximity of rock samples to faults, and effects of surface weathering.

We refer to our samples as unaltered and altered for simplicity. Yet, we acknowledge that some other factors may also be involved in the measured changes. The following actions and facts need to be taken into consideration to compare between the altered and unaltered lithofacies:

- Sampling of Entrada Sandstone took place in the same geographical location and same proximity to the leaking fault from different layers in the same stratigraphic succession.
- Sampling of Summerville Siltstone took place in the same stratigraphic layer but at different distance to the fault CO_2 leakage conduit. The proximity to the fault may have resulted in mechanical changes of rock fabric although such changes were not detectable in thin section petrography. Fracture networks resulted in extended reach of the CO_2-charged brine alteration beyond the reaction depth that it would be expected in a non-fractured medium [Kampman et al., 2016].
- Sampling of the Mancos Shale sample took place in similar stratigraphic layers but at different distances from the fault (Table 1). Similar to Summerville Siltstone, Mancos Shale also exhibits mineralized fracture networks in the proximity of the fault, not present far away from it.

All samples were excavated from beneath the immediate rock face in order to reduce the impact of surface weathering on rock diagenesis. Weathering effects would affect altered and unaltered samples equally. Observed diagenetic differences between altered and unaltered samples are thus attributed to the variable water-rock interaction with distance from the CO_2 leakage fault conduits.

5.3. Outcrop versus subsurface alteration path: conceptual differences, DEM-BPM model results and the role of effective stresses

5.3.1. Effects of cement dissolution in outcrop rocks versus the subsurface

Outcrop and near surface rocks are subjected to relatively small levels of mean effective and deviatoric stress. Hence mineral dissolution mostly results in enlarged porosity without compromising the integrity of the rock formation. Likewise, mineral dissolution experiments at low effective mean stress and/or no deviatoric stress, may principally result in enlargement of pores or cavities [McDuff et al. 2010; Carroll et al., 2013; Aman et al., 2017]. Grain dissolution, contact cement dissolution and creation of secondary porosity can lead to decreases of cohesive strength, fracture toughness and size of yield stress locus. Examples include the results of Section 3 (naturally altered rocks near surface) and others by [Bemer and Lombard, 2010; Major et al., 2014; Rinehart et al., 2016; Sun et al., 2016a].

Let us explore the effect of cement mineral dissolution at low effective stress with numerical simulation and the model developed for Entrada Sandstone in Section 4. We limit our DEM numerical simulations to Entrada Sandstone because of its granular nature and because we assume straight-forward chemo-mechanical alteration (mostly dissolution of contact cement). Sun et al., in review investigate effects of pore-filling mineral dissolution. Figure 9a shows a schematic of the numerical model. The model parameters are the same as those in Section 4. The digital sample is a 1.5 mm cube containing 8,332 particles and 24,410 bonds. For the outcrop case we assume constant and isotropic effective stress σ_{iso} = 0.5 MPa (about 50 m of burial). Cement bond size parameter λ decreases from 0.8 to 0.4 over time representing cement dissolution at bonds due to interaction with CO_2-acidified water. A change of parameter λ from 0.8 to 0.4 results in a linear strain $\Delta\varepsilon_{zz} < 1\times10^{-5}$ (Figure 9b). The horizontal stress does not change because of the assumed constant stress boundary condition.

5.3.2. Effects of cement dissolution under subsurface 1-D strain and high-effective stress conditions

Mineral dissolution in rocks under high levels of mean and deviatoric stress –such as in reservoir rocks in CO_2 storage sites– does not necessarily mirror the changes observed at near-surface conditions. If stresses are high enough, dissolution of cement and mineral grains can lead to grain crushing, pore collapse, grain rearrangement and loss of porosity instead of increase of porosity and rock weakening. Such loss of porosity can lead to reservoir compaction, decreases of the fracture (stress) gradient, and stress redistribution in the reservoir rock and adjacent rock strata [Shin et al., 2008; Kim and Santamarina, 2014; Jung and Espinoza, 2017].

We created a DEM-BPM model to investigate the chemo-mechanical alteration path that mimics contact cement dissolution under in-situ stressed condition. The model is the same as in Section 5.3.1 but subjected to different boundary conditions. We explore two cases: (1) cement dissolution under constant effective stress σ_{iso} = 50 MPa, and (2) cement dissolution under 1-D vertical strain conditions with constant effective vertical stress equal to σ_{zz} = 50 MPa (overburden of about 3.5 km in an on-shore sedimentary basin with hydrostatic pore pressure). 1-D vertical strain (zero lateral strain) conditions more accurately represent the stress-strain path of long and relatively thin formations in the subsurface [Segall et al., 1998, Espinoza et al., 2015, Dudley et al., 2016, Shovkun and Espinoza, 2018].

1. In the isotropic case, a change of parameter λ from 0.8 to 0.4 results in a linear strain $\Delta\varepsilon_{zz} = 2.9\times10^{-4}$ (Figure 9b). The horizontal stress does not change because of assumed constant boundary conditions.
2. In the 1-D strain case, fixed walls constrain the digital cubical sample in the horizontal direction during bond-size reduction (fixed displacement) and permit quantifying horizontal stresses. The initial horizontal stresses $\sigma_{xx} = \sigma_{yy}$ ~49 MPa are about the same as the vertical stress, representing a near isotropic initial stress state. A change of parameter λ from 0.8 to 0.4 results in a linear vertical strain $\Delta\varepsilon_{zz} = 3.7\times10^{-4}$ (Figure 9b). The decrease of cement bond size over time also results in horizontal stress relaxation of about 10%, i.e., $\Delta\sigma_{xx} = \Delta\sigma_{yy}$ ~ -5 MPa. Models investigating dissolution of entire particles in uncemented granular media yield similar conclusions [Shin et al. 2008; Cha and Santamarina, 2014].

Our simulation results support the premise that CO_2 alteration induced by mineral dissolution may have different impacts on outcrops and subsurface reservoirs due to overburden stress and 1-D vertical strain conditions.

5.4. Field-scale implications of chemo-mechanical coupled processes in CO_2 reservoirs

The previous section provides evidence of compaction and horizontal stress relaxation due to load-bearing cement dissolution, as expected in some rocks exposed to CO_2-acidified brine. Significant strains caused by chemo-mechanical weakening (leading to compaction, shearing of wellbore casing, and subsidence) have yet to be observed in CO_2 injection field projects. Chemo-mechanical alteration under subsurface conditions can also result in stress changes in addition to those caused by pore pressure changes. For example, the Decatur site shows unexpected microseismic activity in the Mt. Simon reservoir sandstone and underlying basement rock well after CO_2 injection and related pore pressure transients [Bauer et al., 2016]. In addition to pore pressure alterations, which are critical for safe CO_2 storage [Verdon et al., 2014; Jung et al., 2018], we hypothesize that one other possible mechanism for the seismic activity could be horizontal stress transfer to critically stressed basement faults arising from chemo-mechanical weakening of the overlying reservoir rock. Similar stress transfer mechanisms from the reservoir to adjacent formations occur during reservoir depletion, gas desorption from organic-rich rock, and rock cooling [Segall, 1989; Segall and Fitzgerald, 1998; Goulty, 2003; Espinoza et al., 2015; Paluszny et al., 2017]. Small changes of minimum horizontal stress would have a direct impact on fault stability for normal and strike-slip regimes but would not destabilize faults in reverse-faulting regime.

Dissolution of load-bearing mineral can also contribute to reduction of fracture toughness and thresholds for subcritical fracture propagation in both the reservoir and caprock [Major et al., 2014]. Mineral dissolution also results in changes of rock strength and large-strain behavior – as observed in core scale experiments and DEM simulations. Even though dissolution may cause undesired strains and changes of stress in the reservoir, a large-scale change from brittle to ductile behavior could help avoid strain localization, high permeability channels, and rapid release of elastic energy (as induced seismicity) from the altered rocks. Conversely, mineral precipitation could lead to rock strengthening and fracture sealing.

The extent of coupled chemo-mechanical alterations is proportional to the extent of chemical reactions in the reservoir rocks. The injection of a finite amount of anhydrous CO_2 in a given reservoir results in distinct areas of CO_2-brine mixtures throughout the reservoir, with varying levels of bulk CO_2 saturation,

brine saturation, salinity and pH [Kumar et al., 2005; Kneafsey and Pruess, 2010; Rohmer et al., 2016]. Seepage through localized regions may result in flow of a significant number of pore volumes of CO_2-charged fluids, a situation unlikely in most of the CO_2 reservoir domains at depth (with exception of near-wellbore regions and areas of potential localized leaks). Hence, changes of rock properties (and expected changes of strain/stress) next to leakage paths represent end-members of chemo-mechanical alteration.

6. Conclusions

- This study shows experimental evidence of (1) reduction of stiffness, strength, and brittleness of Entrada sandstone and Summerville siltstone, and (2) increase of stiffness in Mancos shale after alteration with CO_2-charged brine.
- We tested outcrop rock samples that have been altered by fault-controlled percolation of CO_2-charged brines at the Little Grand Wash Fault, Crystal Geyser site, and compared against samples of lesser CO_2-brine alteration. Because of low overburden stress, rocks samples may have not undergone a directly coupled chemo-mechanical diagenesis. A different scenario is expected in a target storage formation under in-situ stresses and subsurface boundary conditions.
- Numerical modeling with the DEM-BPM method confirms loss of cementation as one likely variable for observed sandstone weakening. Coupled chemo-mechanical simulations predict reservoir compaction and horizontal stress relaxation induced by chemically-induced loss of cementation under in-situ conditions.
- The comparison of unaltered and altered lithofacies by CO_2 is appealing and instructive to elucidate long-term alteration mechanisms. However, several factors can affect a direct comparison. These include (in order of priority for our study): (1) distance to fault gouge and induced faulting strains and fractures, (2) location in the sequence stratigraphy and spatial variability in horizontal direction, (3) the presence of events that postdate CO_2 alteration, and (4) surface weathering.
- Extensive flow of CO_2-charged brine, such as in localized leakage pathways, can significantly alter the deformational behavior and mechanical properties of some sedimentary rocks.
- Early identification of CO_2-susceptible rocks and understanding of particle level mechanisms is helpful to avert undesired emergent phenomena from chemical and mechanical coupled interactions.

Acknowledgments

This work was supported as part of the Center for Frontiers of Subsurface Energy Security, an Energy Frontier Research Center funded by the U.S. Department of Energy, Office of Science, Basic Energy Sciences under Award DE-SC0001114. The research was conducted at The University of Texas at Austin and at Sandia National Laboratories. Sandia National Laboratories is a multimission laboratory managed and operated by National Technology and Engineering Solutions of Sandia, LLC., a wholly owned subsidiary of Honeywell International, Inc., for the U.S. Department of Energy's National Nuclear Security Administration under contract DE-NA-0003525.

This paper describes objective technical results and analysis. Any subjective views or opinions that might be expressed in the paper do not necessarily represent the views of the U.S. Department of Energy or the United States Government.

References

Alsalman, M. E., Myers, M. T., & Sharf-Aldin, M. H. (2015). Comparison of Multistage to Single Stage Triaxial Tests. In 49th US Rock Mechanics/Geomechanics Symposium. American Rock Mechanics Association.

Aman M. D., Ilgen A., Major J., Eichhubl P., Dewers T., Espinoza D. N. (2017). "Characterization of chemo-mechanical alteration in CO_2 storage rocks via scratch testing", Greenhouse Gases: Science and Technology. doi:10.1002/ghg.1726.

ASTM. (2010). D7012–10: Standard test method for compressive strength and elastic moduli of intact rock core specimens under varying states of stress and temperatures. Annual Book of ASTM Standards, American Society for Testing and Materials, West Conshohocken, PA, 495-498.

Bakker, E., Hangx, S. J., Niemeijer, A. R., & Spiers, C. J. (2016). Frictional behaviour and transport properties of simulated fault gouges derived from a natural CO_2 reservoir. International Journal of Greenhouse Gas Control, 54, 70-83.

Bauer, R. A., Carney, M., & Finley, R. J. (2016). Overview of microseismic response to CO_2 injection into the Mt. Simon saline reservoir at the Illinois Basin-Decatur Project. International Journal of Greenhouse Gas Control, 54, 378-388.

Bemer, E., & Lombard, J. M. (2010). From injectivity to integrity studies of CO_2 geological storage-chemical alteration effects on carbonates petrophysical and geomechanical properties. Oil & Gas Science and Technology–Revue de l'Institut Français du Pétrole, 65(3), 445-459.

Benavente, D., García, M. A., García, J., Sánchez-Moral, S., & Ordóñez, S. (2004). Role of pore structure in salt crystallisation in unsaturated porous stone. Journal of crystal growth, 260(3), 532-544.

Burnside, N. M., Shipton, Z. K., Dockrill, B., and Ellam, R. M., 2013, Man-made versus natural CO_2 leakage: A 400 k.y. history of an analogue for engineered geological storage of CO_2: Geology, v. 41, no. 4, p. 471-474.

Carroll, S., Hao, Y., Smith, M., & Sholokhova, Y. (2013). Development of scaling parameters to describe CO_2–rock interactions within Weyburn-Midale carbonate flow units. International Journal of Greenhouse Gas Control, 16, S185-S193.

Cha, M., & Santamarina, J. C. (2014). Dissolution of randomly distributed soluble grains: post-dissolution k 0-loading and shear. Géotechnique, 64(10), 828-836.

Chiodini, G., Frondini, F., & Ponziani, F. (1995). Deep structures and carbon dioxide degassing in central Italy. Geothermics, 24(1), 81-94.

Dockrill, B., and Shipton, Z. K., 2010, Structural controls on leakage from a natural CO_2 geologic storage site; central Utah, U.S.A: Journal of Structural Geology, v. 32, no. 11, p. 1768-1782.

Doelling, H. H. 2002. Interim Geologic Map of the San Rafael Desert 30' x 60 ' Quadrangle, Emery and Grand Counties, Utah. Salt Lake City: Utah Geological Survey.

Duan, Z., & Sun, R. (2003). An improved model calculating CO_2 solubility in pure water and aqueous NaCl solutions from 273 to 533 K and from 0 to 2000 bar. Chemical geology, 193(3), 257-271.

Eichhubl, P., Taylor, W. L., Pollard, D. D., & Aydin, A. (2004). Paleo-fluid flow and deformation in the Aztec Sandstone at the Valley of Fire, Nevada—Evidence for the coupling of hydrogeologic, diagenetic, and tectonic processes. Geological Society of America Bulletin, 116(9-10), 1120-1136.

Espinoza, D. N., & Santamarina, J. C. (2012). Clay interaction with liquid and supercritical CO_2: the relevance of electrical and capillary forces. International Journal of Greenhouse Gas Control, 10, 351-362.

Espinoza, D. N., Pereira, J. M., Vandamme, M., Dangla, P., & Vidal-Gilbert, S. (2015). Desorption-induced shear failure of coal bed seams during gas depletion. International Journal of Coal Geology, 137, 142-151.

565 Fernandez, A. L., & Santamarina, J. C. (2001). Effect of cementation on the small-strain parameters of
566 sands. Canadian Geotechnical Journal, 38(1), 191-199.
567 Fredd, C. N., & Fogler, H. S. (1998). Influence of transport and reaction on wormhole formation in porous
568 media. AIChE journal, 44(9), 1933-1949.
569 Gale, J. F., Reed, R. M., & Holder, J. (2007). Natural fractures in the Barnett Shale and their importance for
570 hydraulic fracture treatments. AAPG Bulletin, 91(4), 603-622.
571 Gaus, I., Azaroual, M., & Czernichowski-Lauriol, I. (2005). Reactive transport modelling of the impact of
572 CO_2 injection on the clayey cap rock at Sleipner (North Sea). Chemical Geology, 217(3), 319-337.
573 Goulty, N.R., 2003. Reservoir stress path during depletion of Norwegian chalk oilfields. Pet. Geosci. 9, 233–
574 241.
575 Gunter, W. D., Perkins, E. H., and Hutcheon, I. (2000). "Aquifer disposal of acid gases: Modelling of water-
576 rock reactions for trapping of acid wastes." Applied Geochemistry, Vol. 15, No. 8, pp. 1085-1095.
577 Hangx, S. J. T., Spiers, C. J., & Peach, C. J. (2010). The effect of deformation on permeability development
578 in anhydrite and implications for caprock integrity during geological storage of CO_2. Geofluids,
579 10(3), 369-387.
580 Hangx, S., Bakker, E., Bertier, P., Nover, G., & Busch, A. (2015). Chemical–mechanical coupling observed
581 for depleted oil reservoirs subjected to long-term CO_2-exposure–A case study of the Werkendam
582 natural CO_2 analogue field. Earth and Planetary Science Letters, 428, 230-242.
583 Heath, J. E., Lachmar, T. E., Evans, J. P., Kolesar, P. T., and Williams, A. P., 2009, Hydrogeochemical
584 characterization of leaking, carbon dioxide-charged fault zones in east-central Utah, with
585 implications for geological carbon storage: Geophysical Monograph, v. 183, p. 147-158.
586 Jung, H., Singh, G., Nicolas Espinoza, D., & Wheeler, M. F. (2017). An Integrated Case Study of the Frio CO_2
587 Sequestration Pilot Test for Safe and Effective Carbon Storage Including Compositional Flow and
588 Geomechanics. In SPE Reservoir Simulation Conference. Society of Petroleum Engineers.
589 Kaszuba, J. P., Janecky, D. R., and Snow, M. G. (2005). "Experimental evaluation of mixed fluid reactions
590 between supercritical carbon dioxide and NaCl brine: Relevance to the integrity of a geologic
591 carbon repository." Chemical Geology, Vol. 217, Nos. 3-4, pp. 277-293.
592 Kharaka, Y. K., Cole, D. R., Hovorka, S. D., Gunter, W. D., Knauss, K. G., & Freifeld, B. M. (2006). Gas-water-
593 rock interactions in Frio Formation following CO_2 injection: Implications for the storage of
594 greenhouse gases in sedimentary basins. Geology, 34(7), 577-580.
595 Kim, S., & Santamarina, J. C. (2014). CO_2 geological storage: hydro-chemo-mechanical analyses and
596 implications. Greenhouse Gases: Science and Technology, 4(4), 528-543.
597 Kneafsey, T. J., & Pruess, K. (2010). Laboratory flow experiments for visualizing carbon dioxide-induced,
598 density-driven brine convection. Transport in porous media, 82(1), 123-139.
599 Kumar, A., Noh, M. H., Ozah, R. C., Pope, G. A., Bryant, S. L., Sepehrnoori, K., & Lake, L. W. (2005). Reservoir
600 simulation of CO_2 storage in aquifers. SPE Journal, 10(03), 336-348.
601 Lake, L. W. (1996). Enhanced oil recovery. Prentice Hall. 600 p.
602 Lee, H. P., Olson, J. E., Holder, J., Gale, J. F., & Myers, R. D. (2015). The interaction of propagating opening
603 mode fractures with preexisting discontinuities in shale. Journal of Geophysical Research: Solid
604 Earth, 120(1), 169-181.
605 Liteanu, E., Spiers, C. J., & De Bresser, J. H. P. (2013). The influence of water and supercritical CO_2 on the
606 failure behavior of chalk. Tectonophysics, 599, 157-169.
607 Major, J.R., Eichhubl, P., Dewers, T.A., Urquhart, A.S., Olson, J.E., Holder, J., 2014. The Effect of CO_2-
608 Related Diagenesis on Geomechanical Failure Parameters: Fracture Testing of CO_2-Altered
609 Reservoir and Seal Rocks from a Natural Analog at Crystal Geyser, Utah, ARMA. American Rock
610 Mechanics Association, Minneapolis, MN, pp. 1-5. https://www.onepetro.org/conference-
611 paper/ARMA-2014-7463

McDuff, D., Shuchart, C. E., Jackson, S., Postl, D., & Brown, J. S. (2010). Understanding wormholes in carbonates: Unprecedented experimental scale and 3-D visualization. In SPE Annual Technical Conference and Exhibition. Society of Petroleum Engineers.

McGrail, B. P., Schaef, H. T., Glezakou, V.-A., Dang, L. X., and Owen, A. T. (2009). "Water reactivity in liquid and scCO_2 phase: Has half the story been neglected?." Energy Procedia GHGT-9, Vol. 1, pp. 3415-3419.

Oudinot, A., Koperna, G., Philip, Z., Liu, N., Heath, J., Wells, A., Young, G., Wilson, T., 2011. CO_2 injection performance in the Fruitland Coal Fairway, San Juan Basin: results of a field pilot. SPE J. 16, 864–879.

Pacala, S., & Socolow, R. (2004). Stabilization wedges: solving the climate problem for the next 50 years with current technologies. science, 305(5686), 968-972.

Paluszny, A., Salimzadeh, S., Tempone, P., & Zimmerman, R. W. (2017, August). Evaluating Natural Fracture Growth in Shale Caprocks During Cold CO_2 Injection at the Heletz Pilot Site. In 51st US Rock Mechanics/Geomechanics Symposium. American Rock Mechanics Association.

Pearce, J. M., Holloway, S., Wacker, H., Nelis, M. K., Rochelle, C., & Bateman, K. (1996). Natural occurrences as analogues for the geological disposal of carbon dioxide. Energy Conversion and Management, 37(6), 1123-1128.

Ramos, M., Espinoza, D. N., Torres-Verdin, C., Grover T. Use of shear-wave anisotropy to quantify the onset of stress-induced microfracturing. Geophysics – In press.

Rimmelé, G., Barlet-Gouédard, V., & Renard, F. (2010). Evolution of the petrophysical and mineralogical properties of two reservoir rocks under thermodynamic conditions relevant for CO_2 geological storage at 3 km depth. Oil & Gas Science and Technology–Revue de l'Institut Français du Pétrole, 65(4), 565-580.

Rinehart, A. J., Dewers, T. A., Broome, S. T., & Eichhubl, P. (2016). Effects of CO_2 on mechanical variability and constitutive behavior of the Lower Tuscaloosa Formation, Cranfield Injection Site, USA. International Journal of Greenhouse Gas Control, 53, 305-318.

Rohmer, J., Pluymakers, A., & Renard, F. (2016). Mechano-chemical interactions in sedimentary rocks in the context of CO_2 storage: Weak acid, weak effects?. Earth-Science Reviews, 157, 86-110.

Ross, G. D., Todd, A. C., Tweedie, J. A., & Will, A. G. (1982). The dissolution effects of CO_2-brine systems on the permeability of UK and North Sea calcareous sandstones. In SPE Enhanced Oil Recovery Symposium. Society of Petroleum Engineers.

Rutqvist, J., Rinaldi, A. P., Cappa, F., Jeanne, P., Mazzoldi, A., Urpi, L., Guglielmi, Y. & Vilarrasa, V. (2016). Fault activation and induced seismicity in geological carbon storage–Lessons learned from recent modeling studies. Journal of Rock Mechanics and Geotechnical Engineering, 8(6), 789-804.

Sathaye, K. J., Hesse, M. A., Cassidy, M., & Stockli, D. F. (2014). Constraints on the magnitude and rate of CO_2 dissolution at Bravo Dome natural gas field. Proceedings of the National Academy of Sciences, 111(43), 15332-15337.

Segall, P., & Fitzgerald, S. D. (1998). A note on induced stress changes in hydrocarbon and geothermal reservoirs. Tectonophysics, 289(1), 117-128.

Sharp, J. M. (1975). The Potential of Enhanced Oil Recovery Processes. In Fall Meeting of the Society of Petroleum Engineers of AIME. Society of Petroleum Engineers.

Shin, H., Santamarina, J. C., & Cartwright, J. A. (2008). Contraction-driven shear failure in compacting uncemented sediments. Geology, 36(12), 931-934.

Shovkun, I., & Espinoza, D. N. (2018). Geomechanical implications of dissolution of mineralized natural fractures in shale formations. Journal of Petroleum Science and Engineering, 160, 555-564.

Spycher, N., Pruess, K., & Ennis-King, J. (2003). CO_2-H_2O mixtures in the geological sequestration of CO_2. I. Assessment and calculation of mutual solubilities from 12 to 100 C and up to 600 bar. Geochimica et cosmochimica acta, 67(16), 3015-3031.

660 Stefanou, I., & Sulem, J. (2014). Chemically induced compaction bands: Triggering conditions and band
661 thickness. Journal of Geophysical Research: Solid Earth, 119(2), 880-899.
662 Stumm, W., & Morgan, J. J. (2012). Aquatic chemistry: chemical equilibria and rates in natural waters (Vol.
663 126). John Wiley & Sons.
664 Sun, Y., Aman, M., & Espinoza, D. N. (2016a). Assessment of mechanical rock alteration caused by CO_2–
665 water mixtures using indentation and scratch experiments. International Journal of Greenhouse
666 Gas Control, 45, 9-17.
667 Sun, Z., Espinoza, D. N., & Balhoff, M. T. (2016b). Discrete element modeling of indentation tests to
668 investigate mechanisms of CO_2-related chemomechanical rock alteration. Journal of Geophysical
669 Research: Solid Earth, 121(11), 7867-7881.
670 Sun, Z., Espinoza, D. N., Balhoff, M. T., & Dewers, T. A. Discrete Element Modeling of Micro-scratch Tests:
671 Investigation of Mechanisms of CO_2 Alteration in Reservoir Rocks. Rock Mechanics and Rock
672 Engineering, 1-12.
673 Sun, Z., Espinoza, D. N., Balhoff, M. T., Reservoir rock chemo-mechanical alteration quantified by triaxial
674 tests and implications to fracture reactivation. International Journal of Rock Mechanics and
675 Mining Sciences. In review.
676 Urquhart, A. S. M., 2011, Structural controls on CO_2 leakage and diagenesis in a natural long-term carbon
677 sequestration analogue: Little Grand Wash fault, Utah [MS Thesis]: University of Texas at Austin,
678 437 p.
679 Vanorio, T., Nur, A., & Ebert, Y. (2011). Rock physics analysis and time-lapse rock imaging of geochemical
680 effects due to the injection of CO_2 into reservoir rocks. Geophysics, 76(5), O23-O33.
681 White, W. B., Culver, D. C., Herman, J. S., Kane, T. C., & Mylroie, J. E. (1995). Karst lands. American scientist,
682 450-459.
683 Wigley, M., Kampman, N., Dubacq, B., and Bickle, M., 2012, Fluid-mineral reactions and trace metal
684 mobilization in an exhumed natural CO_2 reservoir, Green River, Utah: Geology.
685 Wilkinson, M., Gilfillan, S. V. M., Haszeldine, R. S., and Ballentine, C. J., 2009, Plumbing the Depths: Testing
686 Natural Tracers of Subsurface CO_2 Origin and Migration, Utah, *in* Grobe, M., Pashin, J. C., and
687 Dodge, R. L., eds., Carbon dioxide sequestration in geological media—State of the science, Volume
688 AAPG studies in geology: Tulsa, OK, American Association of Petroleum Geologists, p. 619–634.
689 Xie, S. Y., Shao, J. F., & Xu, W. Y. (2011). Influences of chemical degradation on mechanical behaviour of a
690 limestone. International Journal of Rock Mechanics and Mining Sciences, 48(5), 741-747.
691 Xu, T., Apps, J. A., & Pruess, K. (2005). Mineral sequestration of carbon dioxide in a sandstone–shale
692 system. Chemical geology, 217(3), 295-318.
693 Yoksoulian, L. E., Freiburg, J. T., Butler, S. K., Berger, P. M., & Roy, W. R. (2013). Mineralogical alterations
694 during laboratory-scale carbon sequestration experiments for the Illinois Basin. Energy Procedia,
695 37, 5601-5611.
696 Zinsmeister, L., Dautriat, J., Dimanov, A., Raphanel, J., & Bornert, M. (2013, January). Mechanical evolution
697 of an altered limestone using 2D and 3D digital image correlation (DIC). In 47th US Rock
698 Mechanics/Geomechanics Symposium. American Rock Mechanics Association.
699

Tables

Table 1. Locations of rock sampling with respect to faults associated with CO_2-charged brine seepage. See satellite image of sampling location in Figure 1.

Lithology	Unaltered	Altered
Entrada Sandstone	JE1: 100 m away from fault (samples ~2 m above JEb1)	JEb1: 100 m away from fault Same place of unaltered sample but different depth
Summerville Siltstone	JS2: 150 m away	JSa1: Beneath travertine mound about 2 m away from fault conduit (foot wall)
Mancos Shale	KM4: 3 km south of fault	KMa1: Few meters from fault beneath travertine mound (hanging wall)

Table 2. List of tested rock samples and test results. Codes in parentheses refer to rock type as in Major et al., 2014. (*) Calculated from weight, bulk volume, and mineralogical composition from Major et al., [in review].

Lithology	Sample ID	Length [cm]	Diameter [cm]	Weight [g]	Porosity* [%]	Triaxial Test Type	Confining Stress σ_3 [MPa]	Axial stress σ_1 (peak) [MPa]	Loading E [GPa]	Loading ν [-]	Unload. E [GPa]	Unload. ν [-]	Mode of Failure
Entrada Sandstone Unaltered (JE1), Composition wt%: Q 55, Feld 7, Cal 7, Dol 7, Clays 24	EU1	5.37	2.544	67.07	8.7	Standard	0.69	70.9	6.1	0.43	16.6	0.19	Brittle, strongly strain-softening
	EU2	5.30	2.535	66.33	7.9	Standard	0.69	50.7	8.9	0.29	21.4	0.16	Brittle, strongly strain-softening
	EU3	5.17	5.537	64.24	8.6	Standard	0.69	82.6	8.9	0.42	19.1	0.12	Brittle, strain-softening
	EU4	5.41	2.542	67.75	8.4	Standard	6.9	115.8	11.2	0.36	23.0	0.17	Brittle, strongly strain-softening
	EU5	5.60	2.542	70.16	8.2	Standard	6.9	102.2	11.0	0.28	23.2	0.14	Brittle with two peaks, strain softening after
	EU7	5.72	2.545	71.97	8.1	Standard	20.7	179.3	17.0	0.25	35.2	0.19	Brittle, strongly strain-softening
Entrada Sandstone Altered (JEb1) Composition wt%: Q 58, Feld 5, Cal 4, Dol 6, Clays 27	EA1	5.47	2.537	65.39	11.7	Standard	0.69	61.7	6.3	0.25	14.6	0.32	Brittle, strongly strain-softening
	EA2	5.39	2.538	64.68	11.4	Standard	0.69	42.9	6.2	0.30	12.9	0.19	Brittle, strongly strain-softening
	EA8	5.33	2.530	63.56	11.4	Standard	0.69	68.7	8.4	0.44	NA	NA	Brittle, strongly strain-softening
	EA4	5.55	2.545	66.6	11.9	Standard	6.9	101.3	9.7	0.34	17.1	0.23	Brittle, strongly strain-softening
	EA7	4.95	0.527	58.88	11.4	Standard	6.9	94.3	11.9	0.27	23.7	0.18	Brittle, strongly strain-softening
	EA3	5.30	2.535	63.37	11.5	Standard	20.7	159.6	13.9	0.18	NA	NA	Brittle, strongly strain-softening
Summerville Siltstone Unaltered (JS2) Composition wt%: Q 59,	SU1	5.19	2.57	68.82	3.5	Standard	0.69	152.3	36.2	0.26	47.3	0.18	Brittle, strongly strain-softening
	SU2	5.04	2.57	66.85	3.6	Standard	0.69	173.0	39.2	0.27	52.2	0.16	Brittle, strongly strain-softening
	SU3	5.21	2.57	67.75	5.3	Multistage	0.69, 6.9, 20.7	158.4, 200.7, 221.5	39.1, 44.0, 43.5	0.20, 0.25, 0.23	54.2, 55.4, 55.8	0.08, 0.10, 0.16	No post-peak information

Feld 8, Cal 23, Clays 10	SU4	5.21	2.57	66.60	6.9	Multistage	0.69, 6.9, 20.7	142.8, 186.1, 227.0	33.4, 40.2, 42.0	0.29, 0.35, 0.27	45.0, 54.7, 55.1	0.15, 0.19, 0.21	No post-peak information
Summerville Siltstone	SA1	5.13	2.57	63.99	9.8	Standard	0.69	26	8.2	0.30	15.4	0.22	Ductile, slightly strain-softening
Altered (JSa1)	SA2	4.70	2.57	58.35	10.1	Standard	0.69	9.4	2.3	0.32	5.3	0.21	Ductile, perfect-plastic followed by strain softening
Composition wt%: Q 32, Feld 17, Cal 38, Clays 13	SA3	4.78	2.57	58.87	10.8	Multistage	0.69, 6.9, 20.7	24.5, 59.2, 116.7	5.2, 8.4, 9.9	0.06, 0.10, 0.13	14.0, 16.8, 22.0	0.14, 0.15, 0.19	No post-peak information
	SA4	4.79	2.57	59.36	10.3	Multistage	0.69, 6.9, 20.7	27.5, 50.6, 109.4	6.7, 7.2, 8.5	0.21, 0.21, 0.20	15.8, 16.5, 22.8	0.29, 0.33, 0.39	No post-peak information
Mancos Shale (KM4)	MU1	3.49	2.507	42.84	6.0	Standard	0.69	51.7	4.9	0.28	15.0	0.13	Brittle with microfractures, strain-hardening
Composition wt%: Q 64, Feld 15, Cal tr Clays 20	MU2	2.89	2.502	35.05	6.7	Loading no-failure	0.69	NA	0.7	0.11	NA	NA	No post-peak information
	MU3	2.90	2.450	34.04	5.9	Loading no-failure	0.69	NA	4.1	0.16	NA	NA	No post-peak information
Mancos Shale Altered (KMa1)	MA1	4.57	2.518	57.46	6.0	Standard	0.69	48.2	8.5	0.27	17.3	0.18	Brittle with multiple microfractures
Composition wt%: Q 16, Feld 9, Cal 50, Dol 1, Clays 20	MA2	3.48	2.519	43.59	6.6	Loading no-failure	0.69	NA	11.85	0.17	17.5	0.22	No post-peak information

714

715

716

717 Table 3. Parameters for the DEM-BPM numerical model

Particle-particle contacts	Bonds
E_c = 4 GPa	E_b = 4 GPa
k_T/k_N = 1	k_T/k_N = 1
μ = 0.5	$\lambda \leq 0.8$
ρ = 2650 kg/m^3	σ_c = 20 MPa
	τ_c = 80 MPa

718

719

Figures

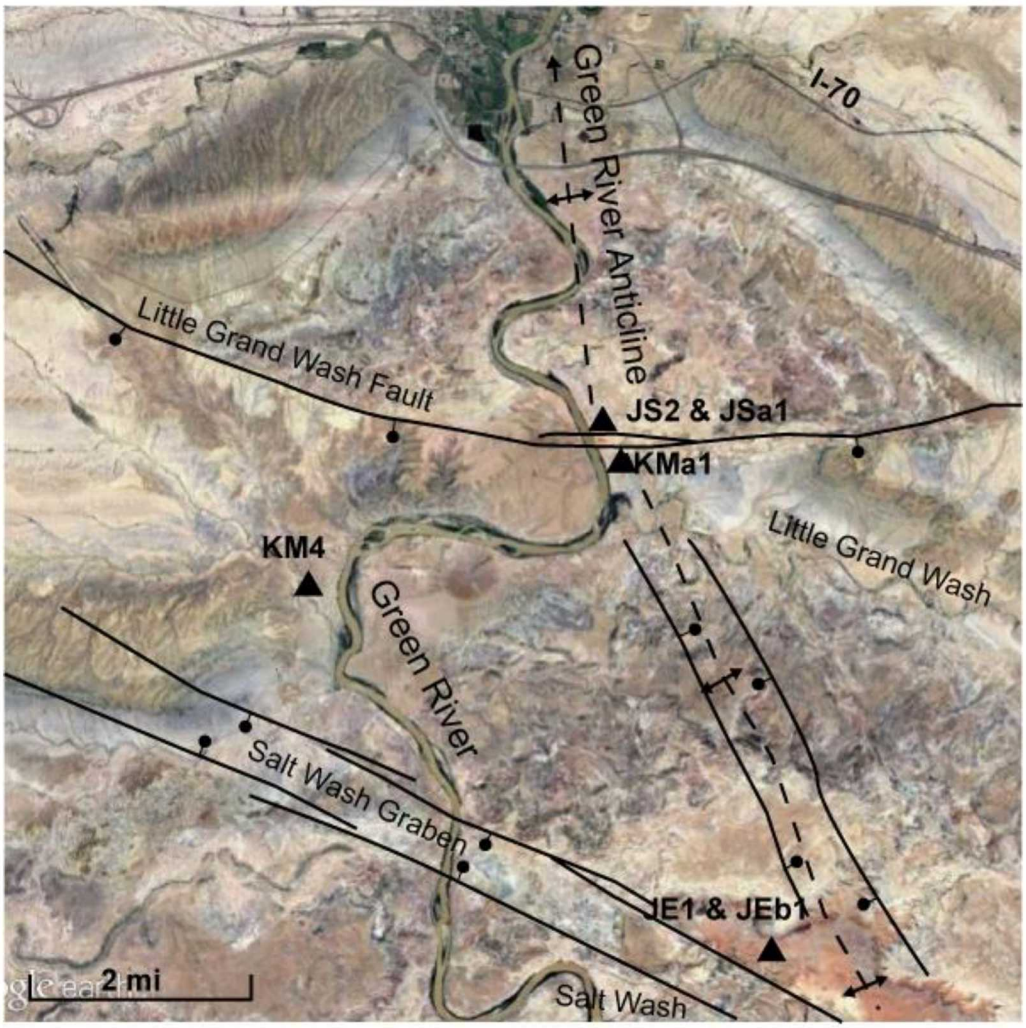

Figure 1. Simplified geologic map and satellite image (credit Google Earth) of the Crystal Geyser field site near Green River, Utah showing location of major structural features and locations of rock sampling. Entrada Sandstone samples were collected from Salt Wash Graben, whereas the other samples described were collected closer to Crystal Geyser and Little Grand Wash Fault.

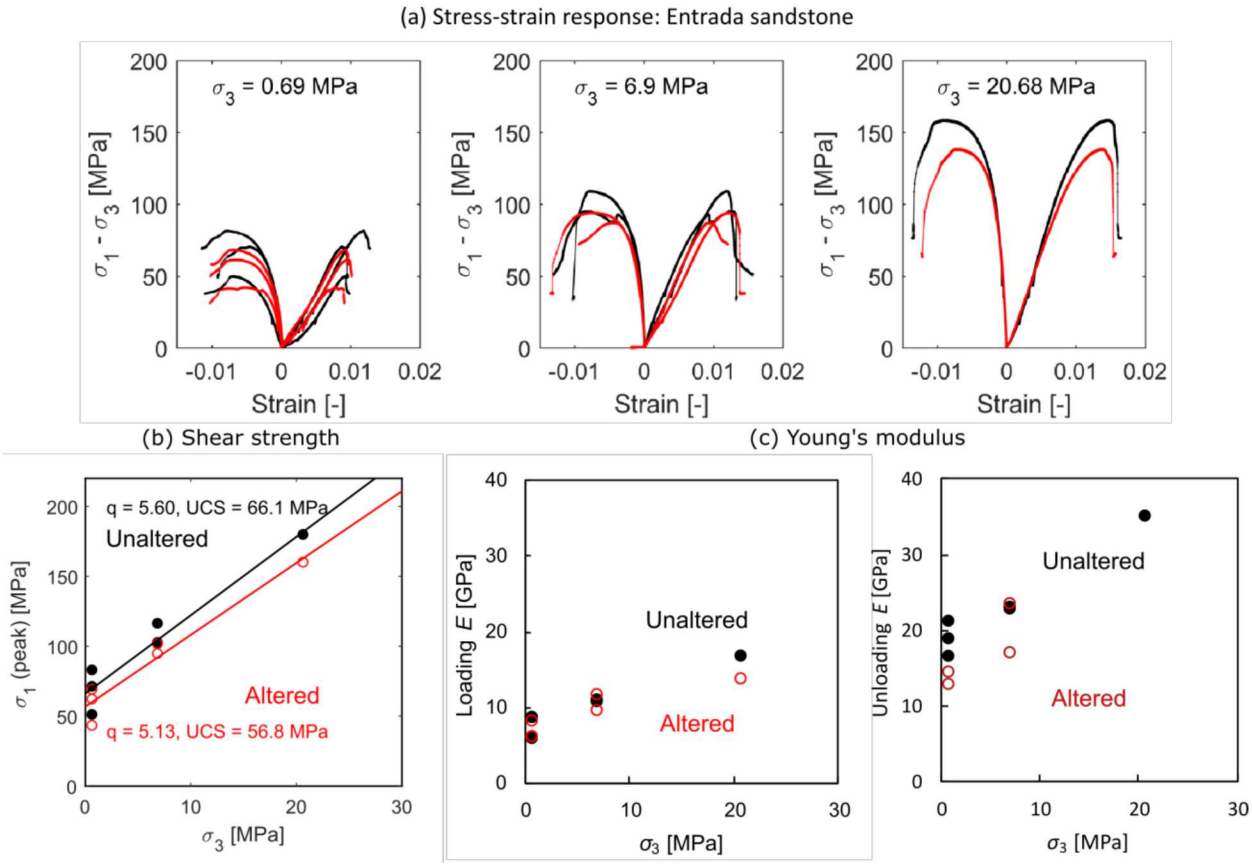

Figure 2. Mechanical response of unaltered (black) and altered (red) Entrada sandstone at various confining stresses σ_3. Axial strains are positive and radial strains are negative. (a) Stress-strain response. (b) Shear strength. (c) Loading and unloading Young's moduli. Altered samples are weaker –in average– and more ductile than unaltered samples.

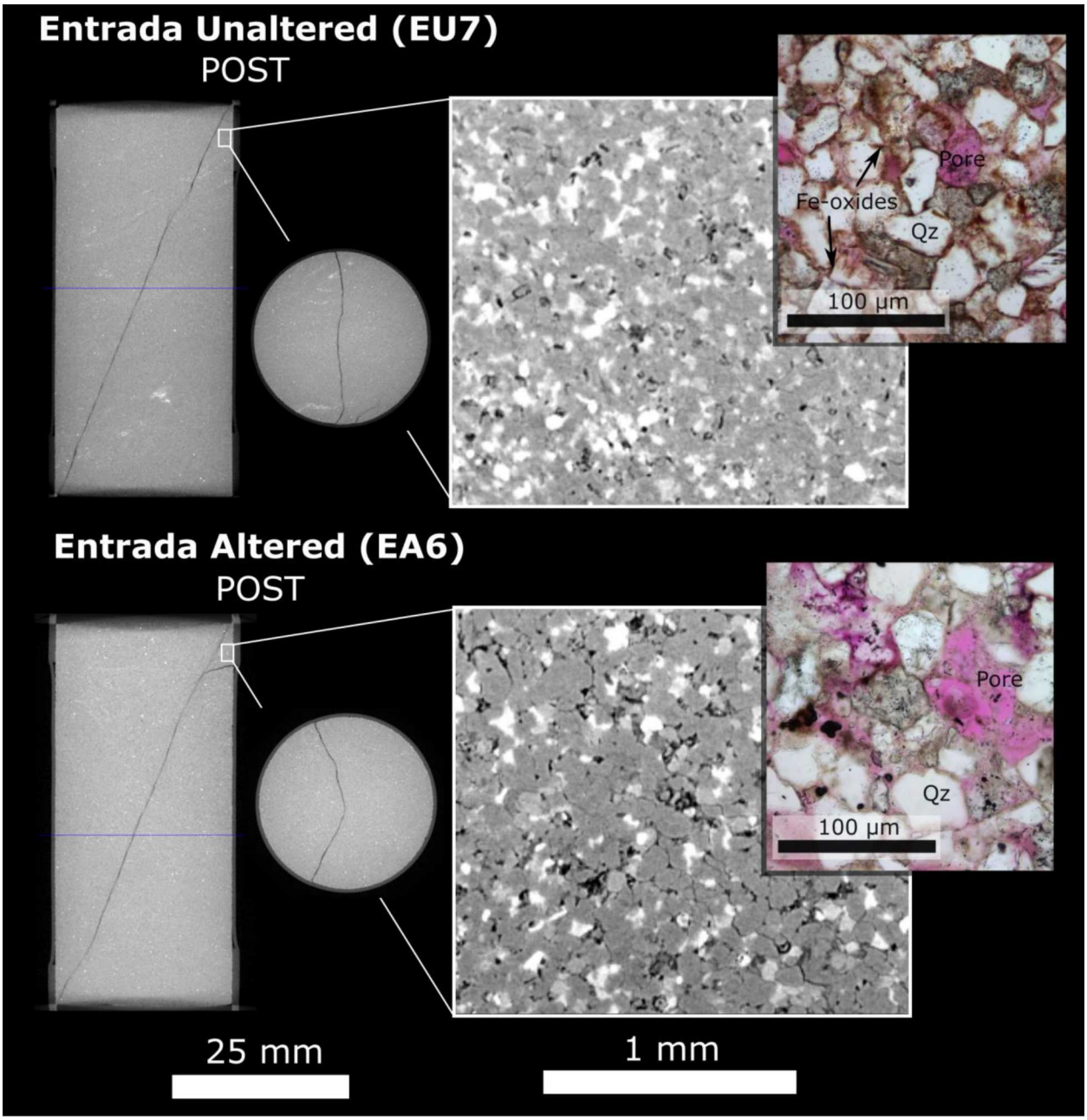

Figure 3. X-ray computed tomography slices of Entrada Sandstone samples post-deviatoric loading (σ_3 = 20.7 MPa). Samples showed clear shear fractures propagating from the ends toward the middle with and without coalescence. Mineral heterogeneities did not seem to affect damage localization. High magnification CT slices shows porosity (black), quartz, carbonates, clay (gray), and detrital mafic clasts (white). Microphotographs highlight the absence of grain-coating cementing iron-oxides in bleached (altered) Entrada Sandstone (pink color represents porosity).

744

745

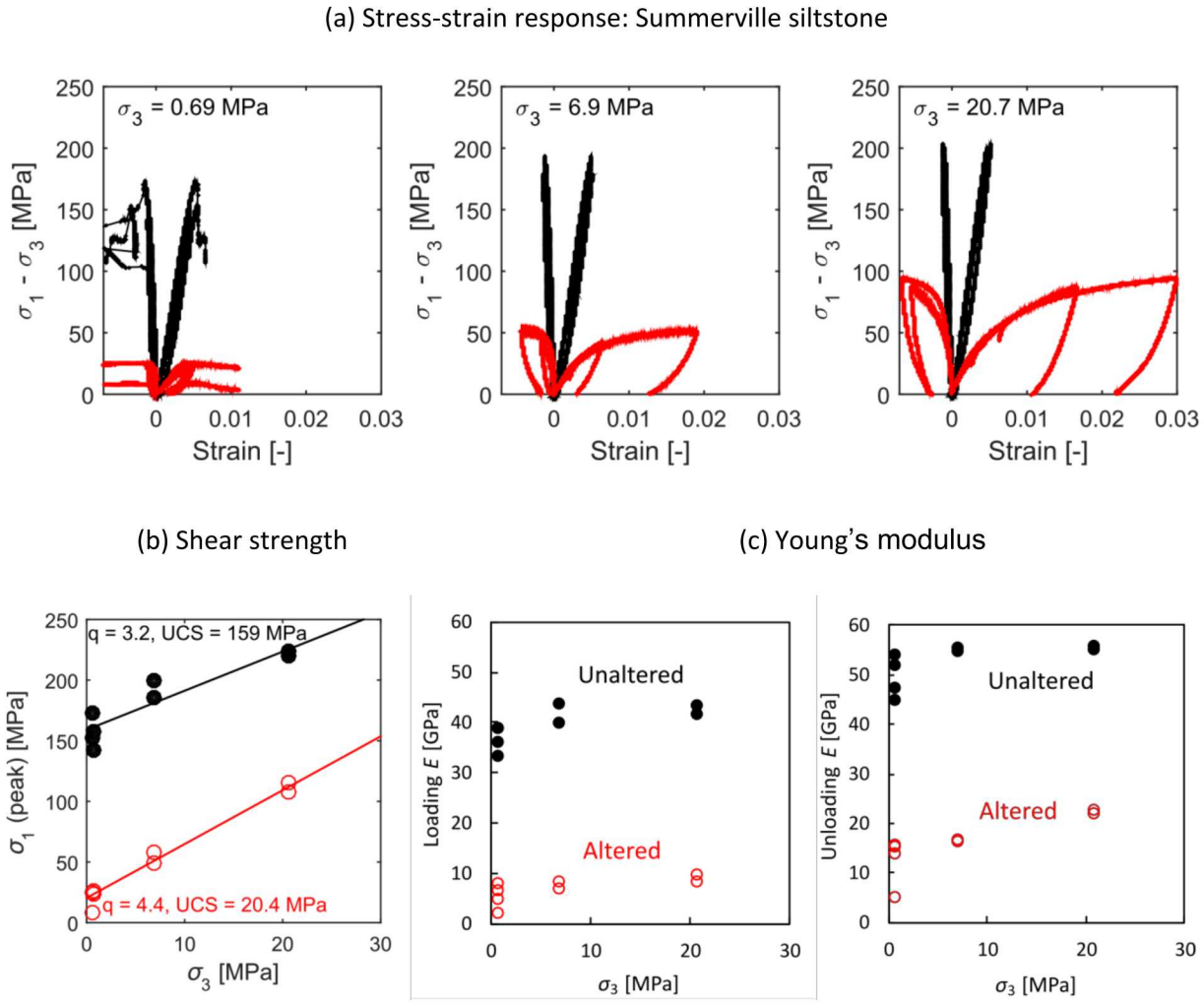

746 Figure 4. Mechanical response unaltered (black) and altered (red) Summerville siltstone at various
747 confining stresses σ_3. Axial strains are positive and radial strains are negative. The multistage
748 experiments finish with deviatoric unloading at a fixed strain rate. (a) Stress-strain response. (b)
749 Shear strength. (c) Loading and unloading Young's moduli. Altered samples show clear weakening
750 and more ductile behavior compared to unaltered samples.

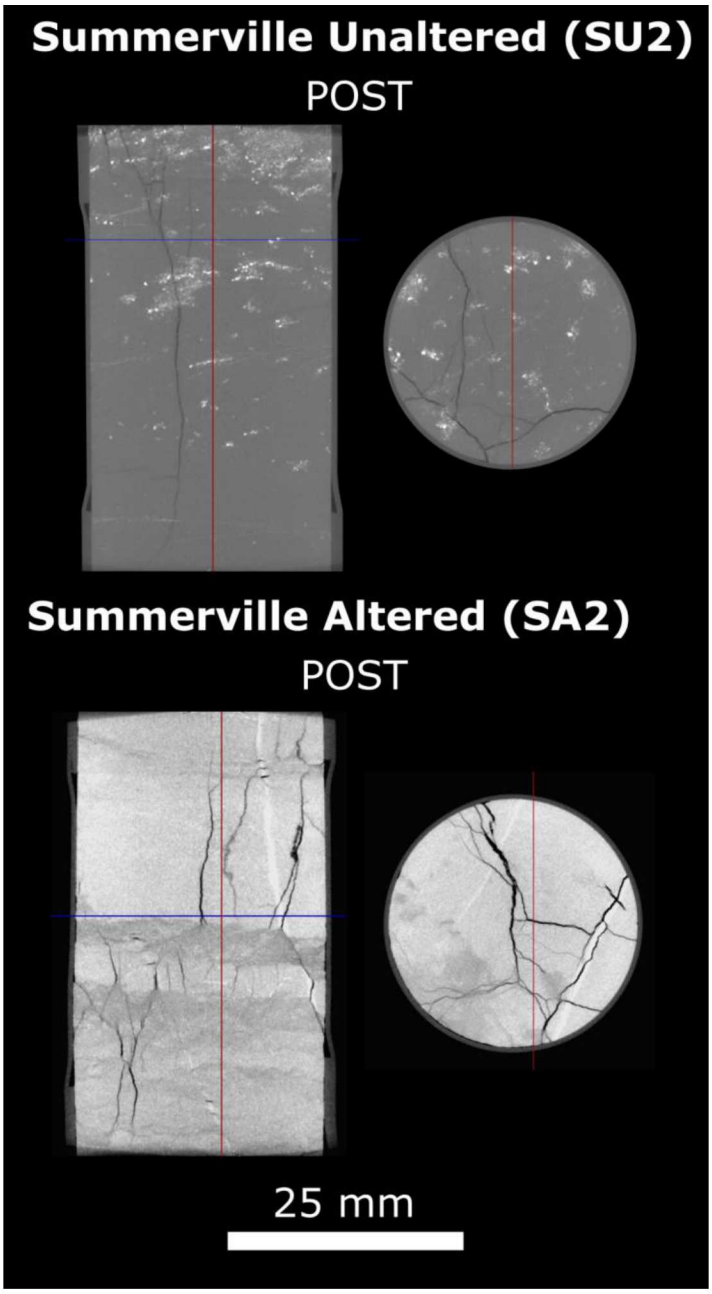

Figure 5. X-ray computed tomography slices of Summerville Siltstone samples post-deviatoric loading (σ_3 = 0.69 MPa). (a) Unaltered samples were mostly homogeneous with patches of detrital mafic clasts (bright mineral phase in CT slices) and exhibited various shear and tension planes upon failure. (b) Altered samples showed marked heterogeneities including layering and partially mineralized fractures, both of which altered strain localization during failure.

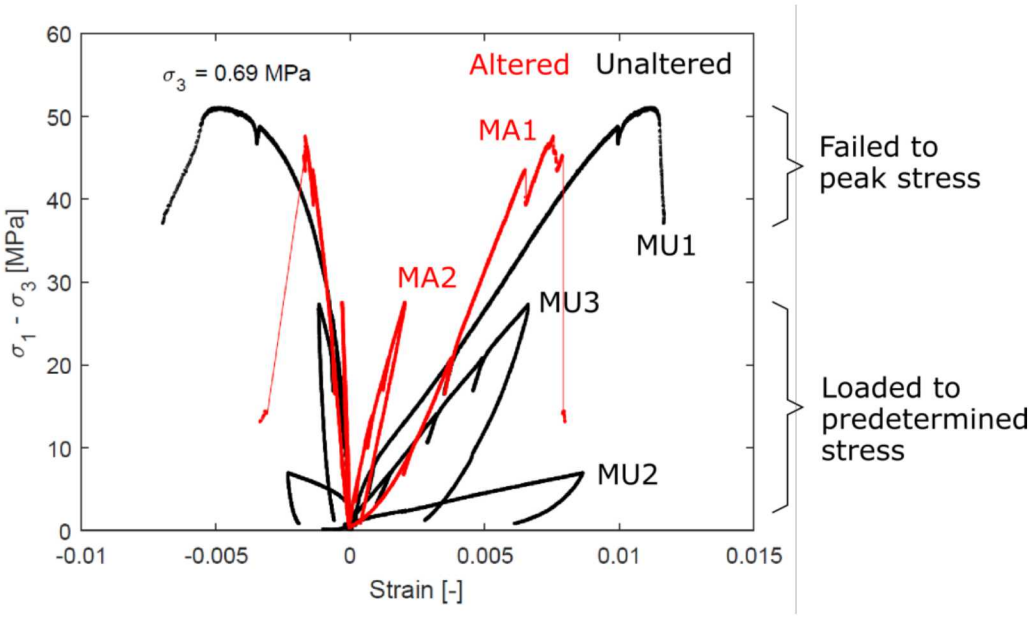

Figure 6. Stress-strain curves for Mancos shale unaltered (black) and altered (red) at an effective confining stress of 0.69 MPa (axial strains are positive and radial strains are negative). Altered samples are stiffer than unaltered samples. MA1 had a height to width ratio equal to 1.39 and therefore peak stress may not be representative of the rock shear strength. MU2, MU3 and MA2 were too short to obtain meaningful strength measurements.

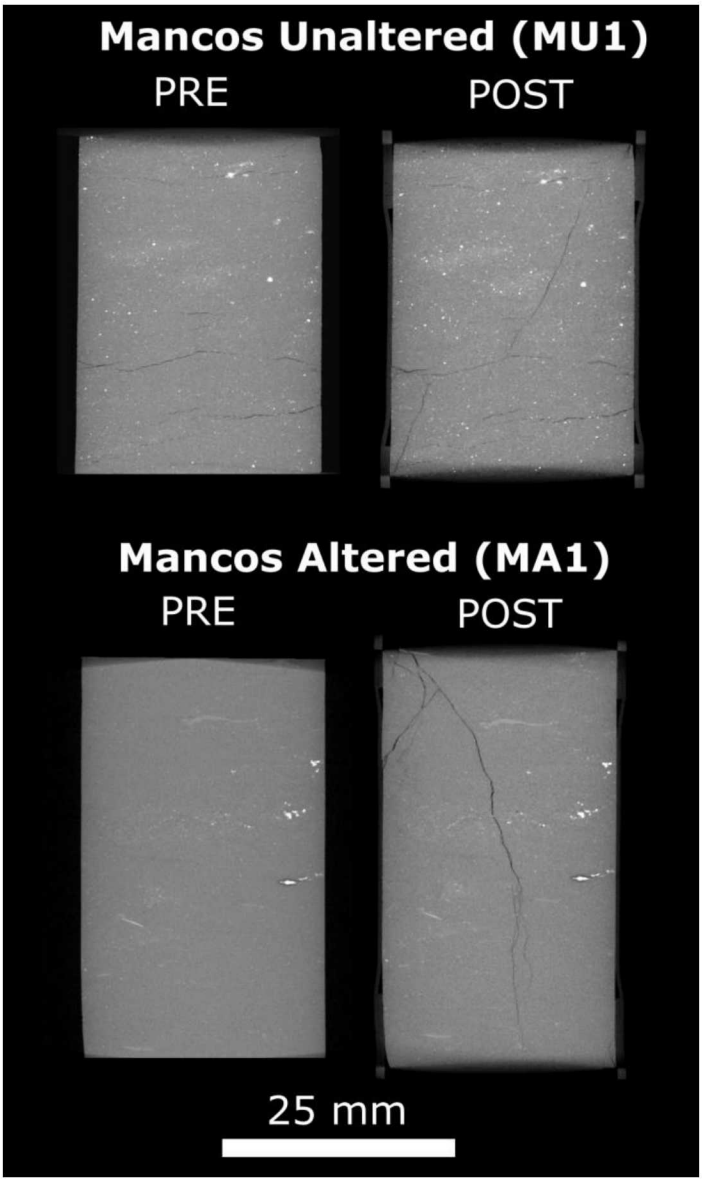

Figure 7. X-ray computed tomography slices of unaltered and altered Mancos shale samples pre- and post-deviatoric loading (σ_3 = 0.69 MPa). Unaltered samples show several pre-existing fractures along laminations which impacted rock stiffness and shear fracture initiation. Bright voxels correspond to pyrite and other Fe-bearing phases.

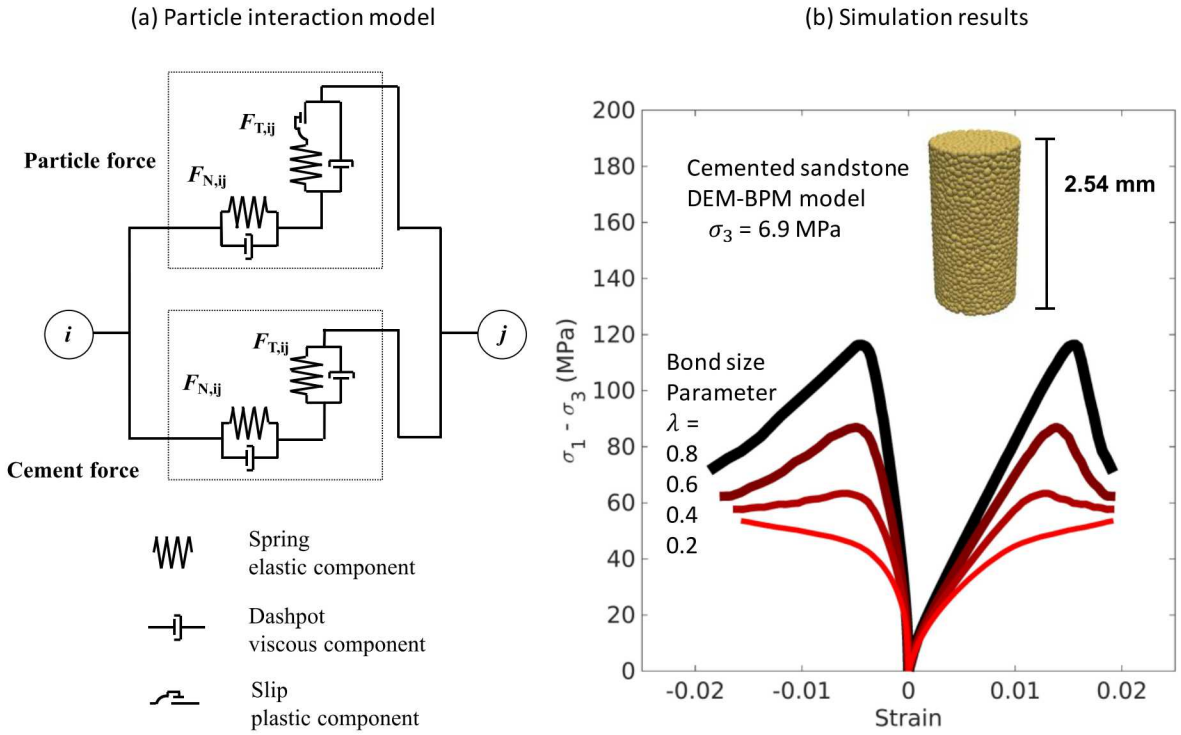

Figure 8. (a) Schematic of DEM model with bonded-particle model. (b) Deformational behavior of digital cemented rock as a function of bond size parameter λ. The average peak deviatoric stress of unaltered Entrada Sandstone at 6.9 MPa of confining stress is 102.1 MPa and unloading Young modulus is 23.1 GPa. The average peak deviatoric stress of altered Entrada Sandstone at the same confining stress is 90.9 MPa and unloading Young modulus is 20.4 GPa. Such change corresponds to a change of bond size parameter λ from 0.8 to ~0.7 in the DEM model at σ_3 = 6.9 MPa.

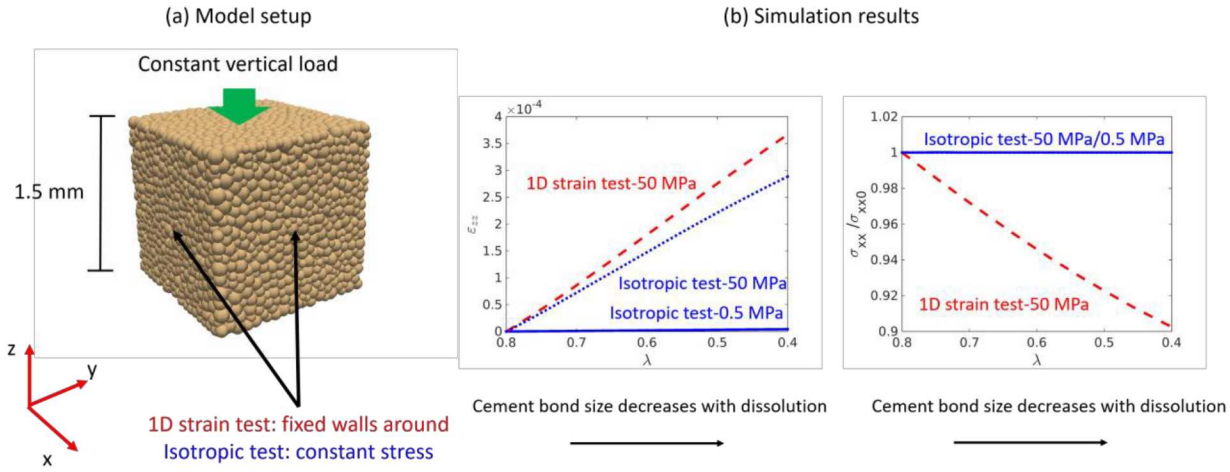

Figure 9. In-situ alteration paths under outcrop and subsurface conditions. A chosen stress of 0.5 MPa represents the outcrop case, while 50 MPa represents the deep subsurface case. (a) Schematic of DEM-BPM model setup and boundary conditions. (b) Variation of vertical strain and horizontal stress as bond size parameter λ decreases (cement dissolution). Negligible strains and changes of stress occur in outcrop conditions in contrast to deep subsurface conditions.

Supporting information

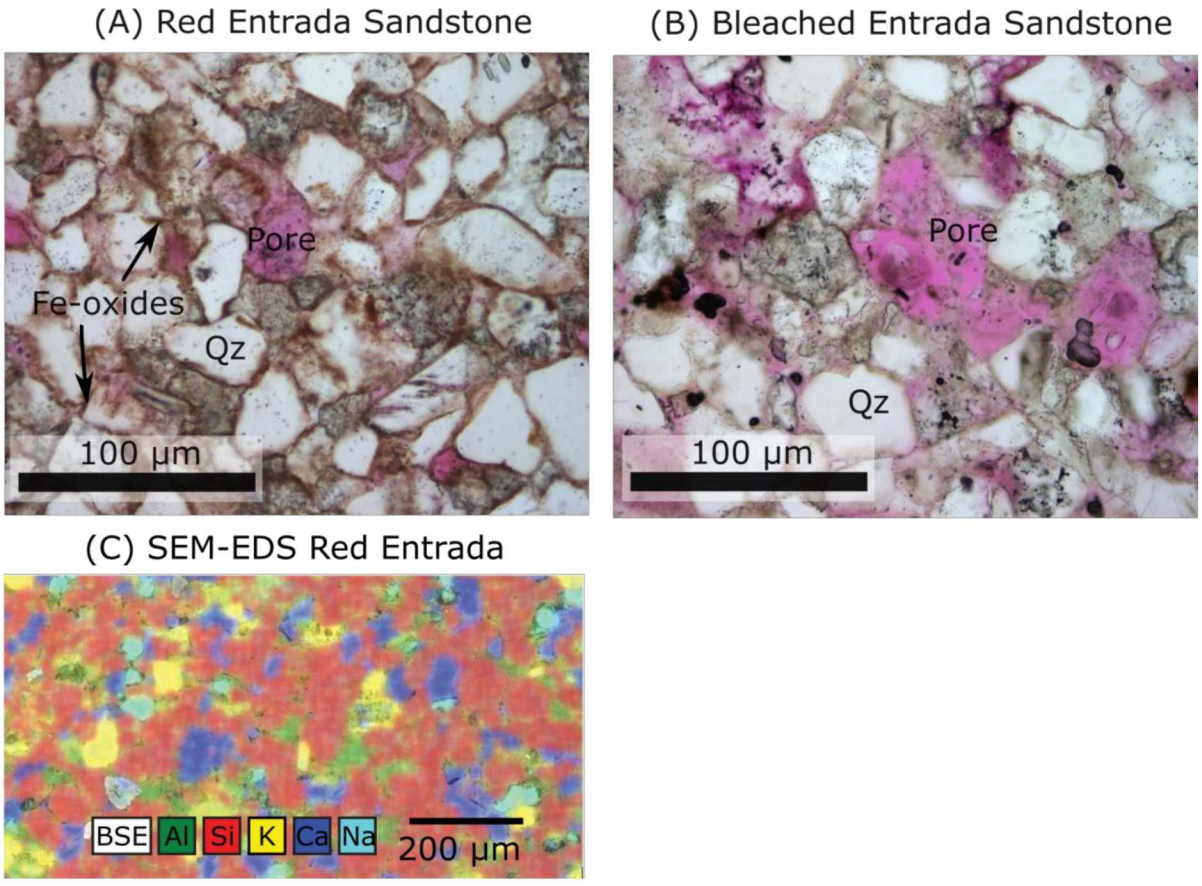

Supporting Information 1. Photomicrographs of red Entrada Sandstone –unaltered (A) and bleached Entrada Sandstone –altered (B). Reddish-brown Fe-oxide grain coats around quartz (Qz) grains are prominent in unaltered Entrada (A) but absent in (B). Pink-dyed epoxy shows porosity. These images support contact-cementation and alteration after bleaching. (C) SEM-EDS image of red Entrada Sandstone. The image highlights a predominantly quartz-feldspar granular skeleton with intergranular carbonates, clays, and other minerals.

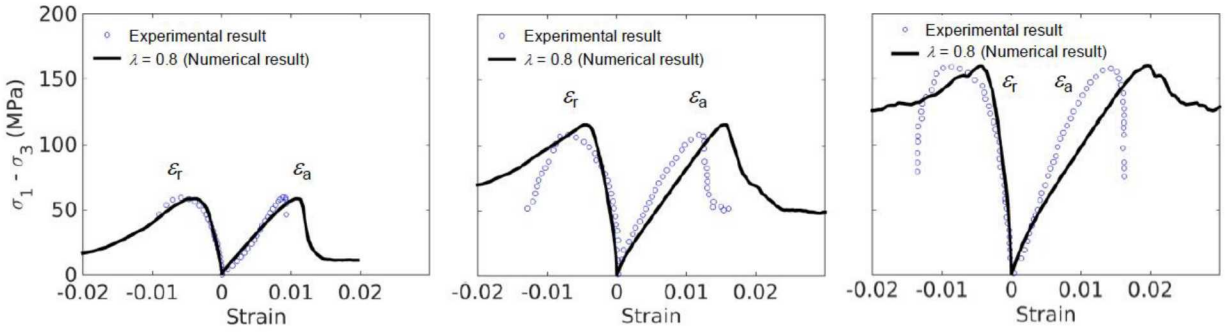

819

820 Supporting Information 2. Prediction of differential stress $\sigma_1 - \sigma_3$ of unaltered Entrada
821 Sandstone with DEM-BPM model. Calibration at σ_3 = 0.69 MPa (a) and blind prediction at
822 σ_3 = 6.9 MPa and σ_3 = 20.7 MPa (b-c). The experimental data represents the average of
823 several samples at each confining stress.

824

825 Supporting Information 3. Summary of mechanical properties of rocks from Crystal
826 Geyser site. (a) Sun et al. [2016a], (b) Major et al., [2014], (c) average from this study.

	Indentation hardness[(a)] [GPa]	**Indentation elastic modulus[(a)] [GPa]**	**Fracture toughness[(b)] [MPa m$^{0.5}$]**	**UCS[(c)] [MPa]**	**Loading E[(c)] [GPa]**	**Unloading E[(c)] [GPa]**
EU (JE1)	0.53 ± 0.23	16.25 ± 3.07	0.68 ± 0.09	66.10	10.85	23.87
EA (JEb1)	0.33 ± 0.09	12.56 ± 1.71	0.42 ± 0.11	56.80	6.25	13.44
Change	-0.38	-0.23	-0.37	-0.14	-0.42	-0.44
SU (JS2)	0.63 ± 0.15	18.28 ± 2.37	2.66 ± 0.29	159.04	39.69	52.46
SA (JAa1)	0.47± 0.21	8.9 ± 4.91	1.64 ± 0.29	20.40	7.05	16.07
Change	-0.25	-0.51	-0.38	-0.87	-0.82	-0.69
MU (KM4)	NA	NA	1.02 ± 0.20	NA	3.23	12.54
MA1 (KMa1)	NA	NA	1.50 ± 0.07	NA	17.24	17.42
Change			+0.47		+4.34	+0.39

827